

A Method for Geometry-Sensitive, CFD Solver Independent Mesh Adaptation

N. Wyman*, P. Galpin** and M. Mirsky*

Corresponding author: nwyman@cadence.com

* Cadence Design Systems, Inc., USA.

** ISimQ Ltd, Canada.

Abstract: A new method for geometry-sensitive, CFD solver-independent mesh adaptation that respects a priori specified boundary layer mesh refinement is presented. The method seeks to control numerical error in the discrete solution by minimizing interpolation error based on the CFD solver discretization. An adaptation sensor, including control over mesh size increases with each adaptation cycle, is used to define a target size field for an updated discrete mesh conforming to the underlying CAD geometry.

Keywords: Mesh Adaptation, Computational Fluid Dynamics.

1 Introduction

Mesh generation and, in particular, fit-for-purpose mesh generation is repeatedly stated as a bottleneck in the CFD simulation workflow. The NASA CFD Vision 2030 Study [1] outlines a basic set of capabilities for CFD by the year 2030 including management of numerical errors and uncertainties along with a high degree of automation for the overall analysis process.

2 Problem Statement

Unstructured meshing can automate much of the mesh generation process; however, controlling numerical errors due to the discrete mesh requires adaptation to the developing solution. A mesh adaptation procedure has been developed which utilizes a pre-defined mesh topology with re-meshing to an updated continuous size field. Adherence to the underlying geometry is maintained and mesh quality is ensured.

From a cubic fit of solution values, an estimate of interpolation error, ε , and thus the truncation error for the CFD solver discretization can be defined [2]:

$$\varepsilon\left(\frac{h}{2}\right) = |\phi^L - \phi^H| = \frac{h}{8} \left| \left[\frac{\partial \phi}{\partial x_2} - \frac{\partial \phi}{\partial x_1} \right] \right| \quad (1)$$

We define a scalar adaptation sensor proportional to the tensor truncation error estimate, ε , as the product of the local edge length raised to an exponent, p , and the difference of the derivatives parallel to the edge vector, h . The exponent, p , provides short edge protection at solution discontinuities (e.g. shocks). Another important property of $p > 1$ is to ensure that multiple scales are resolved in the solution.

$$S = |\vec{h}|^p \left\| \left[\hat{\vec{h}} \cdot \frac{\partial \phi}{\partial x_2} - \hat{\vec{h}} \cdot \frac{\partial \phi}{\partial x_1} \right] \right\| \quad (2)$$

Knowing the current edge length and S value, the value for the updated edge length, h_{Target} , can be directly computed to meet a threshold sensor value, S_{Thresh} , as:

$$h_{Target} = |\vec{h}|^p \sqrt[p]{\frac{S_{Thresh}}{S}} \quad (3)$$

Locations in the current mesh exceeding S_{Thresh} are exported as a sparse, unstructured point cloud which is used by the Pointwise meshing application as input to the continuous size field.

2.1 Controlling Mesh Growth

The selection of the sensor threshold, S_{Thresh} , allows control of the adapted mesh size by utilizing the concept of continuous mesh complexity introduced by Loseille and Alauzet [3]. The ratio of target to current mesh complexity can be computed discretely on the current mesh as:

$$C_r = \frac{\sum_{n=1}^N \left(\frac{1}{|h_{target,n}|^3} \right) V_n}{\sum_{n=1}^N \left(\frac{1}{|h_n|^3} \right) V_n} \quad (4)$$

To achieve a user-specified relative mesh complexity ratio, for example 1.3, we iteratively solve for the appropriate sensor threshold value.

2.1 Selection of Sensor Variable

The adaptation sensor derived above is valid for any solution variable. Selection of the appropriate solution variable is problem dependent and must include consideration of solution objective. For advection dominated flows, good results have been achieved using velocity, vorticity magnitude, and turbulent kinetic energy. External aero calculations work well when selecting Mach Number as the solution variable. The method does allow use of multiple solution variables through superposition.

2.1 Generation of a Conformal Mesh

The Pointwise application uses the original mesh topology combined with the adaptation point cloud to produce a new mesh conformal to the updated size field. In this context, mesh topology means the curve, surface, and volume topology, not cell connectivity. By generating a new mesh from the original mesh topology, as opposed to in situ mesh modification, geometry associativity of the surface mesh is maintained, high-quality orthogonal boundary layers are produced, and overall mesh quality, with respect to size gradation and element shape, remains high.

2.1 Convergence of the Solution-Adapt Cycle

The method is flexible enough to declare convergence in several ways. One qualitative approach is to track the estimated solution truncation error on the current mesh and to declare convergence when the error relative to the solution variable magnitude falls below a user defined threshold. Another possibility is to track the fraction of the mesh where the local sensor exceeds the sensor threshold. When interpolation error becomes equally distributed, a large portion of the mesh ($> 90\%$) will be targeted for refinement. In this scenario, the mesh is undergoing uniform refinement making this condition a reasonable convergence criteria which is independent of scale. Finally, a limit can be placed on the computational resources, e.g. degree of freedom count, of the simulation.

3 Results

The adaptation approach was applied to an impinging jet model, and the results were compared with experimental data and sequences of manually generated structured hex mesh. To demonstrate applicability in a production environment, turbomachinery, automotive, and aeronautical cases are also shown.

3.1 Validation

To validate the mesh adaptation approach, a model of an impinging cold jet on a heated plate was simulated using the ANSYS CFX solver. The geometry and flow conditions have been set to match experiments by Cooper et al. [4] and Baughn et al. [5]. The figure below (Figure 1) shows the 2-D axisymmetric model.

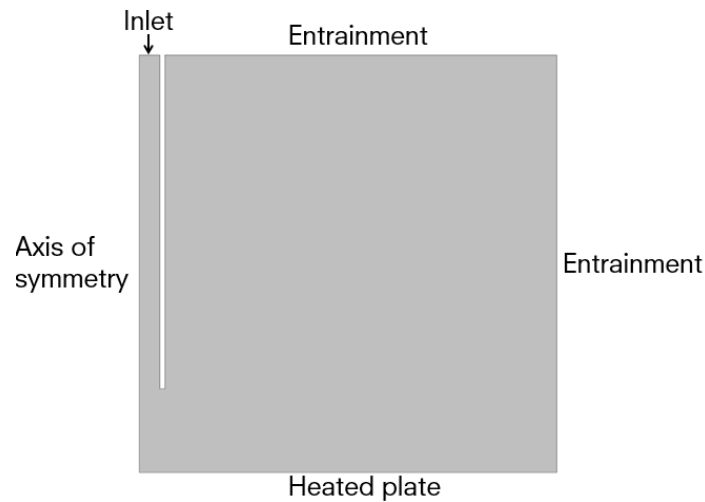


Figure 1: Computational model of jet impingement on flat plate.

The internal pipe diameter D is 26 mm with a pipe wall thickness of 2.912 mm. An inlet velocity profile of air modeled as an ideal gas at 20 °C is specified from a fully developed turbulent pipe flow, such that the Reynolds number based on the pipe diameter was 23,000. The lower plate was heated by specifying a constant temperature of 35 °C. Entrainment conditions (constant total pressure and normal direction for local inflow and static pressure for outflow) were used to permit flow to be entrained at the upper boundary as well as exit smoothly at the right boundary. Because of the low global Reynolds number, the SST transitional intermittency model [6] was used to model the turbulence. The high-resolution advection model was used for all equations, which is a bounded essentially second order numerical scheme. Convergence was declared when the normalized maximum residuals were below 1×10^{-4} , which is close to the single precision round-off level.

Baseline solutions were obtained on a manually created sequence of three hexahedral structured meshes following best practices for such a geometry, where the meshes ranged from 25k to 400k points. The mesh adaptation procedure was then applied to an initial unstructured mesh consisting of 15k points (Figure 2). Turbulent kinetic energy was chosen as the adaptation sensor variable. Mid-way and final adapted meshes are shown in Figure 3 for a value of $p = 3.5$ and $C_r = 1.3$. On the first adaptation cycle, 26.5% of nodes were marked for adaptation. After the 9th adaptation cycle, 94% of the mesh nodes were marked for adaptation hence the cycle was terminated. The mesh from cycle 9 consisted of 330,000 nodes.

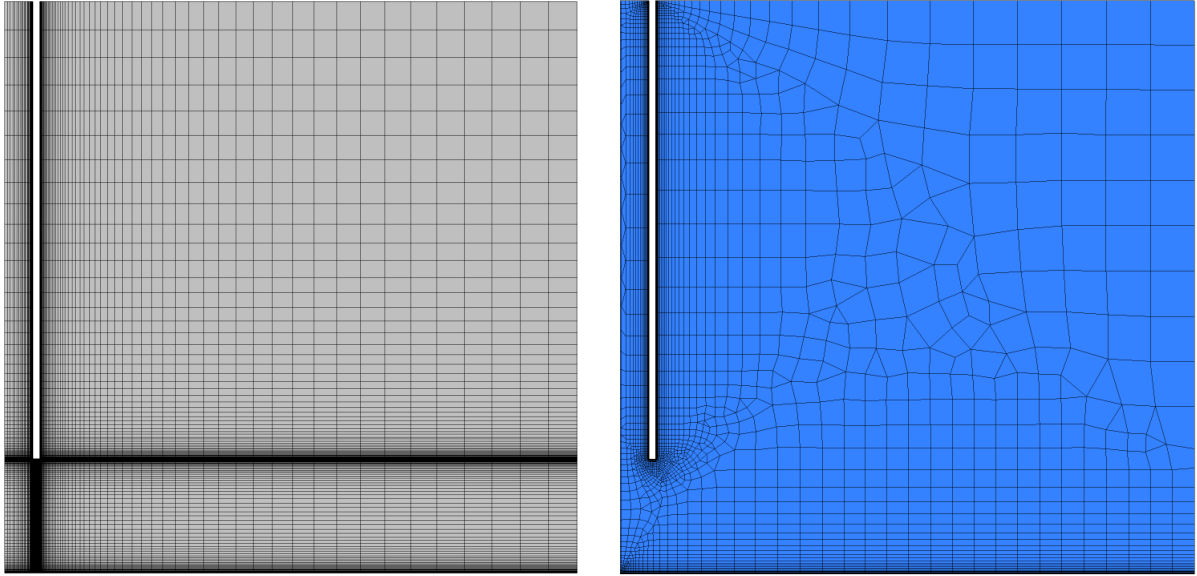


Figure 2: Coarse level hexahedral mesh (left) and initial unstructured hex-dominant mesh (right).

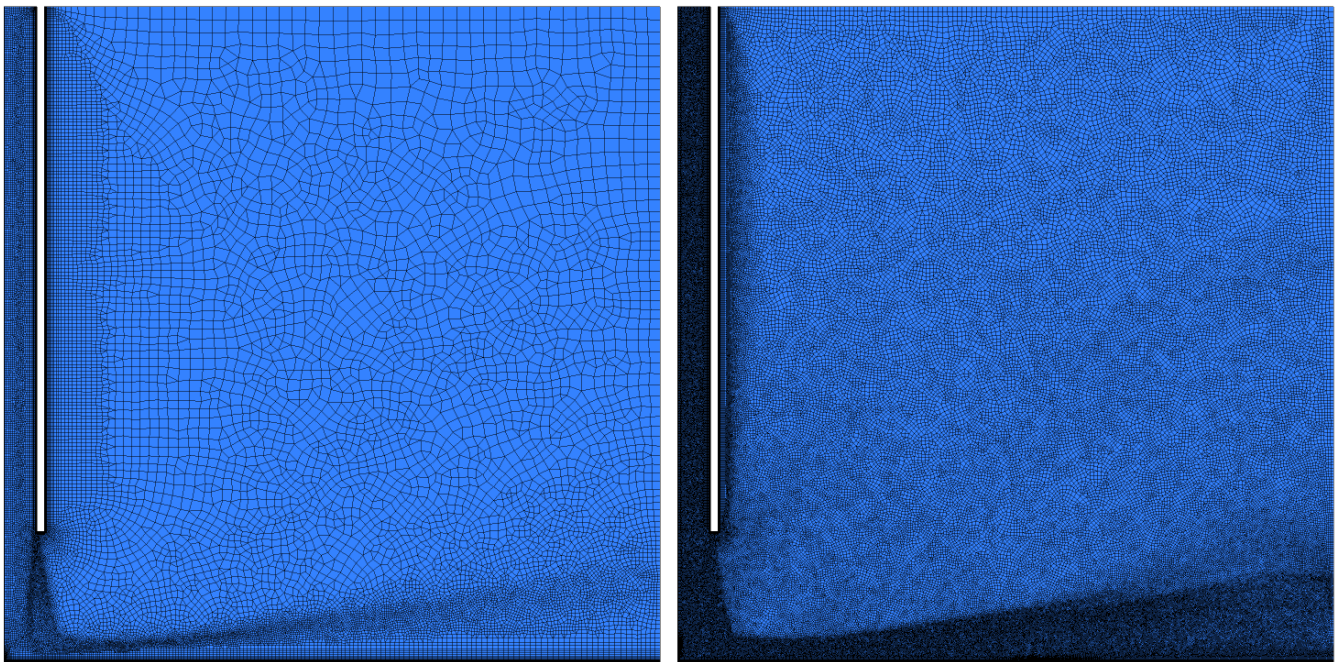


Figure 3: Adapted mesh at Cycle 5 (left) and Cycle 9 (right).

Figure 4 details the mesh size growth with respect to the adaptation cycle. Mesh size grows in a controlled fashion. This is due to the mesh complexity calculation which allows the mesh to grow “in sync” with near physical features found in the updated solution.

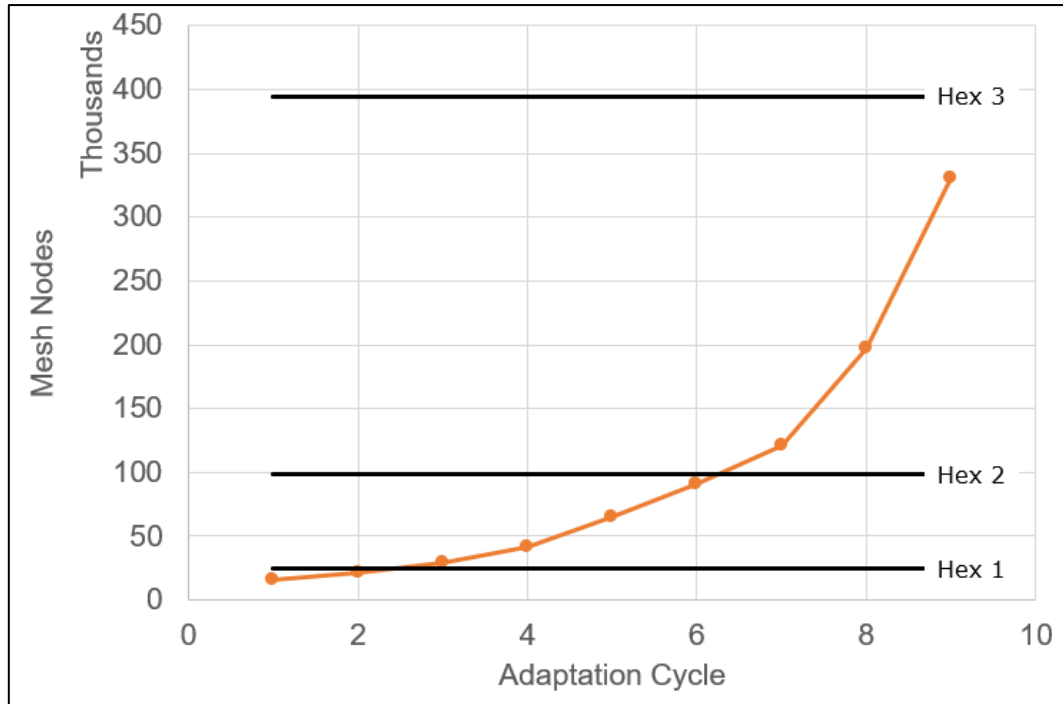


Figure 4: Comparison of mesh point count between the structured hex meshes and the adapted unstructured meshes.

The adapted mesh results compare well with the experimental heat transfer coefficient and with the finest structured hex mesh (Figure 5). Looking closer to the impingement location (Figure 6), it can be noted that the adaptation sequence converges nicely to the experimental data and is as good as, or even better than, the results for the finest structured mesh.

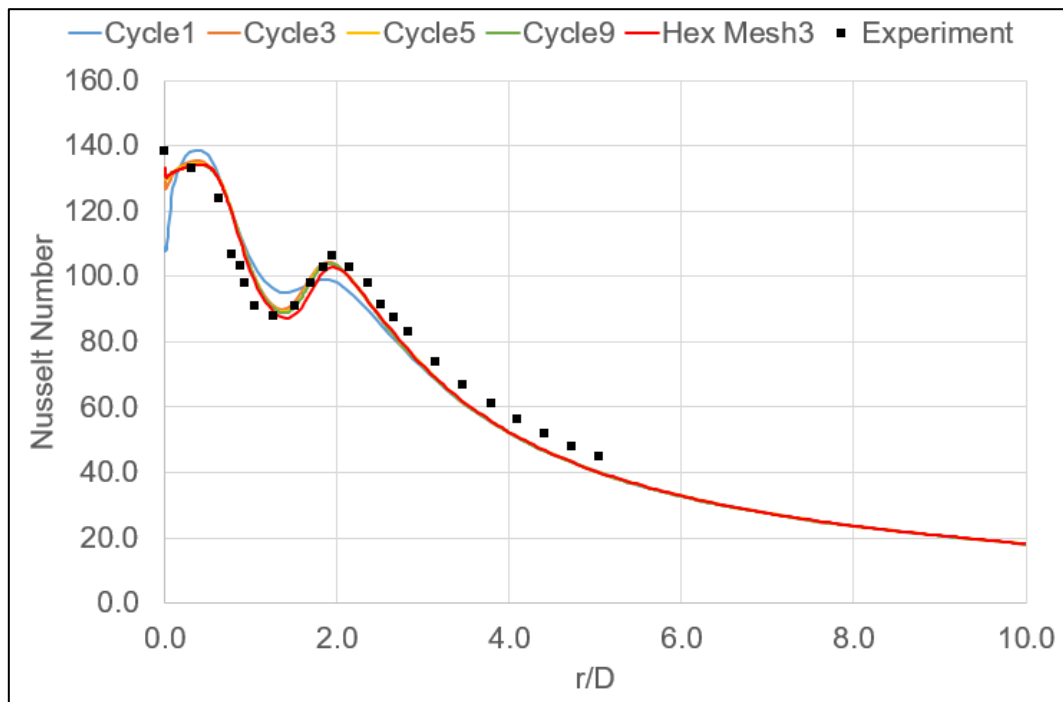


Figure 5: Comparison of heat transfer coefficient for the finest hex mesh and the adapted mesh cycles.

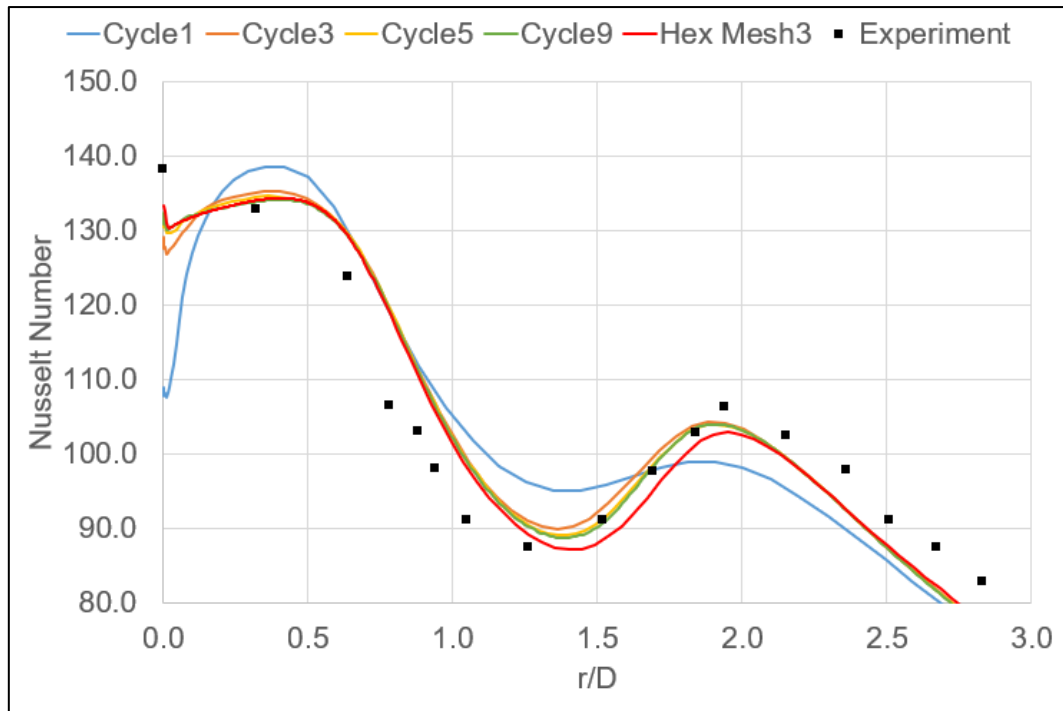


Figure 6: Enlarged view of heat transfer coefficient near the impingement location.

A comparison of calculation wall-clock time for the hex mesh sequence from initial conditions against the adaptation sequence using solution restart is shown in Figure 7. The adaptation method, despite having more computational stages, is competitive with fixed grid run times.

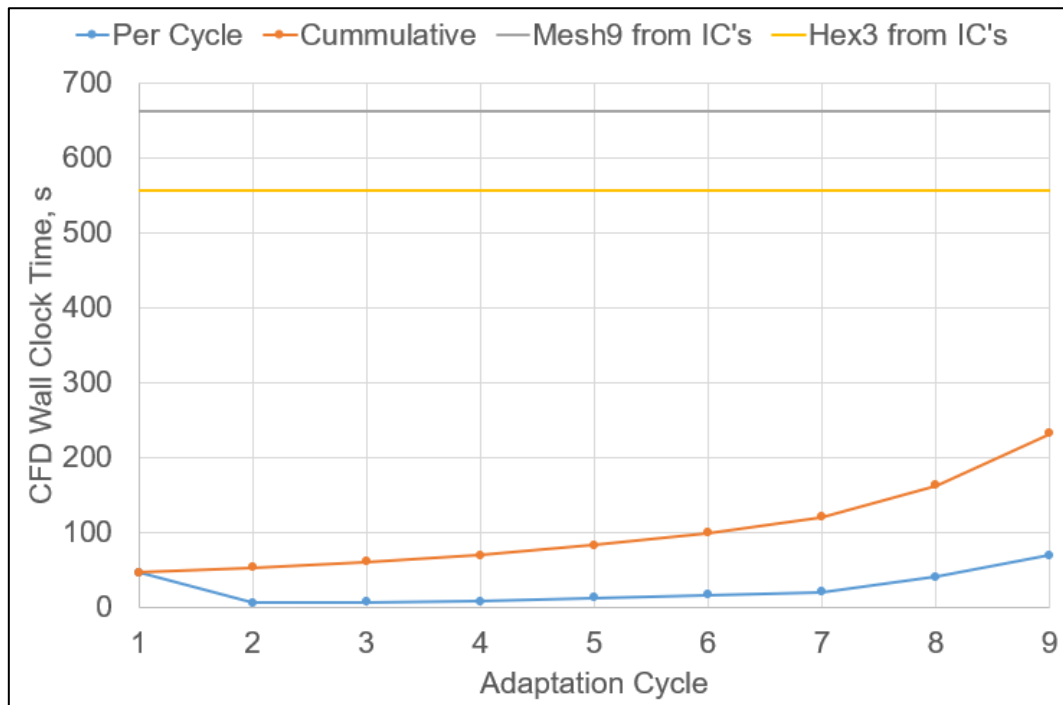


Figure 7: Calculation wall clock times for per-cycle and cumulative adaptation sequence. Horizontal lines represent solution time for final adapted and finest hex meshes from initial conditions.

3.2 Industrial Applications

3.2.1 RWTH Aachen Turbine

A RANS solution of the RWTH Aachen axial turbine [7] rotor was computed using the ANSYS CFX flow solver. Velocity magnitude was chosen as the adaptation sensor variable. The rotational speed of the turbine rotor is 3500 rev/min, and the relative rotor inlet and exit angles are equal to 49.3° and 151.2° , measured with respect to the circumferential direction. For the demonstration, an operating point was chosen with constant inlet total pressure of 169,000 Pa, inlet total temperature of 308 K, and an outlet static pressure of 135,000 Pa. The initial unstructured hex-dominant mesh consisted of 355k points and 610k cells. After 10 cycles, the mesh consisted of 7.8M points. Extrapolation to mesh independent estimates of turbine power and efficiency show only a 0.03% and 0.02% difference from the Cycle 10 results.

The adaptation method is able to resolve relatively weak secondary flow features such as the passage vortices (Figure 8) and hub horseshoe vortex (Figure 9). This behavior is due to the exponent p used in the sensor derivation. A value of $p > 1$ causes adaptation to target relatively large and small solution errors.

Computational time continues to be competitive with best practice hand-made fixed grid solutions. Figure 10 plots solution wall clock time for each solution cycle and cumulative time for all cycles against “cold start” solutions on the cycle meshes. The total time to reach the converged adapted solution is on par with cold start on the final mesh.

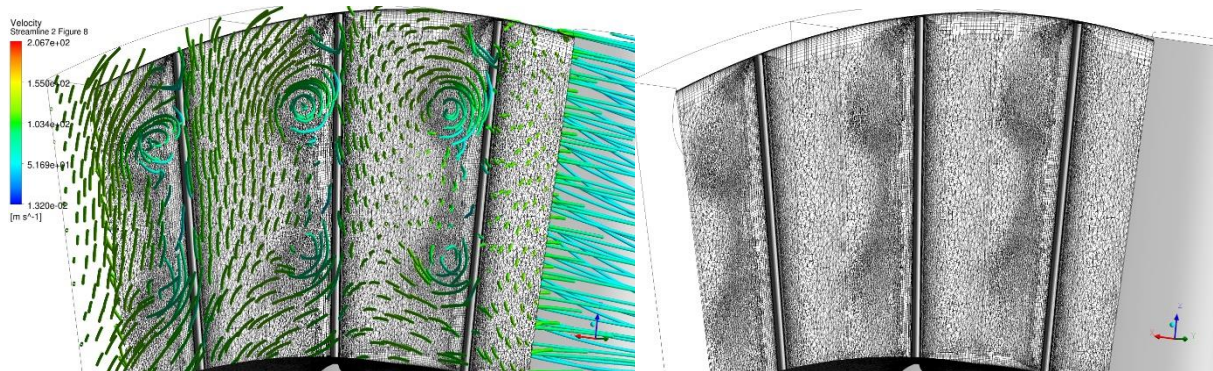


Figure 8: View from downstream of hub and tip passage vortices (left) and adapted mesh (right).

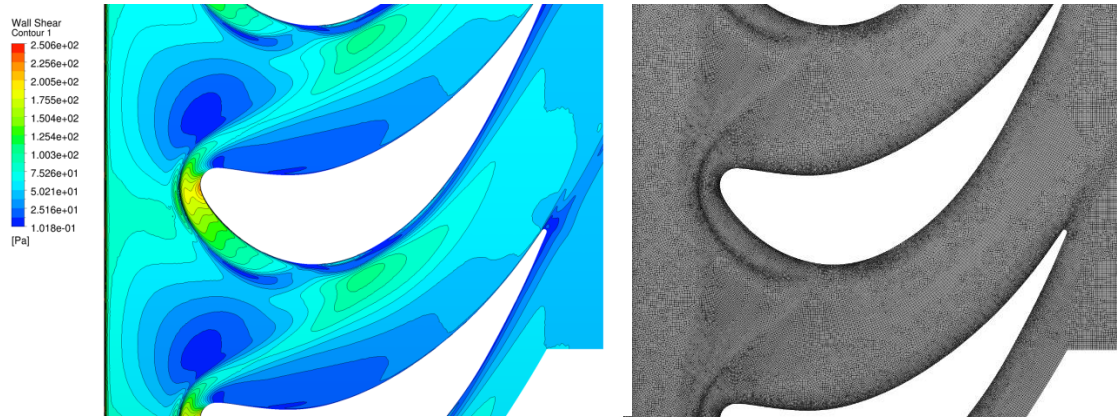


Figure 9: Hub wall shear stress (left) and adapted mesh (right).

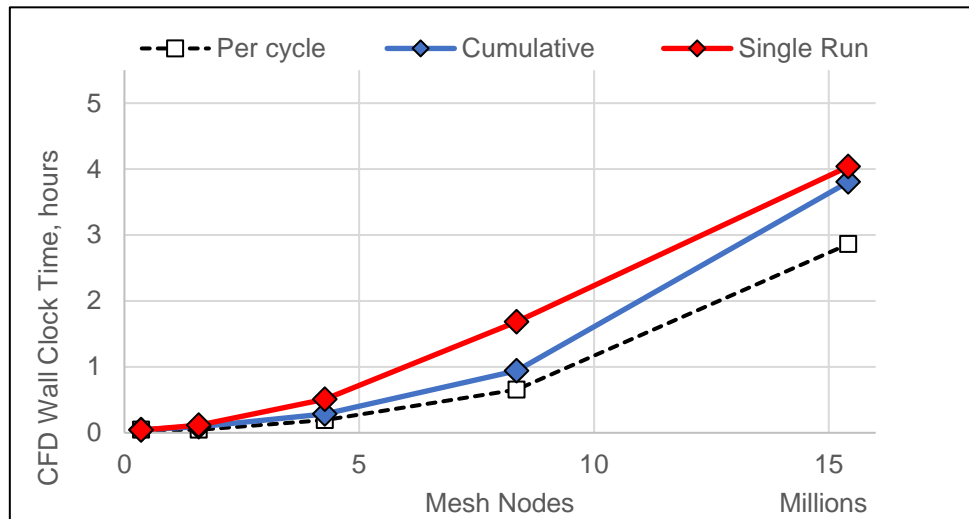


Figure 10: Solution wall-clock time for each solution and cumulative time to final solution compared with single-runs from initial conditions.

3.2.2 Technical University of Munich DrivAer Automobile

An automotive example consists of a RANS solution of the DrivAer Fastback model using the ANSYS CFX flow solver with SST two-equation turbulence model. Velocity magnitude was chosen as the adaptation sensor variable. Six mesh adaptation cycles were performed starting with an initial hex-dominant mesh consisting of 1.6M points. The Cycle 6 mesh contained 24.4M points. Figures 11-12 illustrate adaptation of solution features at the rear of the car. Figure 13 shows mesh size and drag force convergence as a function of adaptation cycle.

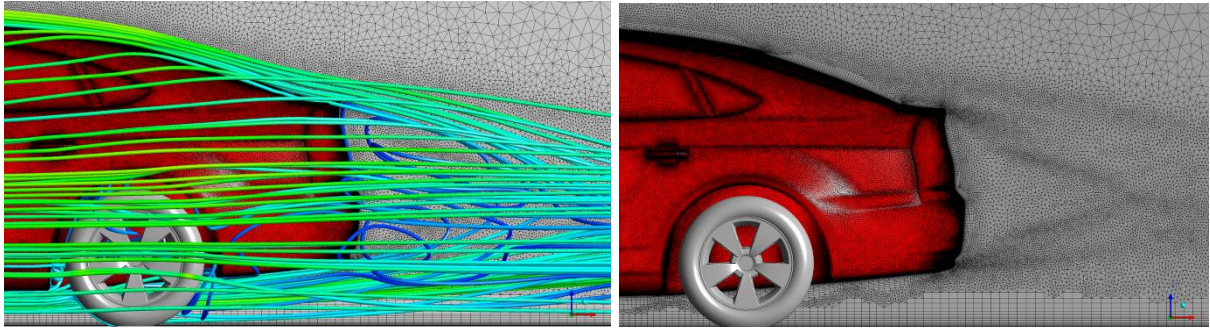


Figure 11: Flow over the car and resolved wake, streamlines (left) and adapted mesh (right).

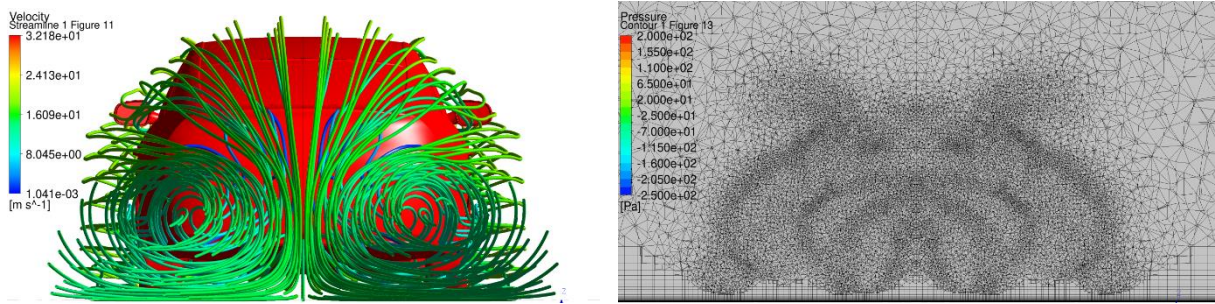


Figure 12: Vortex at the rear of the car, streamlines (left) and adapted mesh (right).

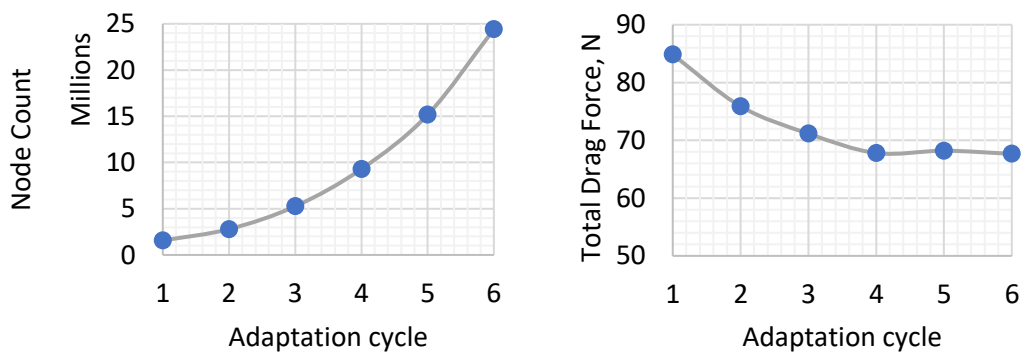


Figure 13: Mesh size and total drag force as a function of mesh adaptation cycle.

3.2.3 DLR F6

An external aero example is given by the SU2 [8] Euler solution of the DLR F6 wing-pylon-nacelle configuration from the 2nd AIAA Drag Prediction Workshop [9]. The flow conditions are $M = 0.75$ at a one degree angle of attack. The adaptation process begins with a hybrid unstructured mesh consisting of 617k points and was run for 13 cycles to produce a final mesh of 3M points. Mach Number was chosen as the adaptation sensor variable. As can be seen in Figure 14-15, wing surface pressure induced by the shock structure is significantly more resolved in the final mesh as compared to the initial mesh. Also apparent in the figure is that geometry associativity is maintained in the surface mesh as evidenced by the better resolved fuselage shape in the final mesh.

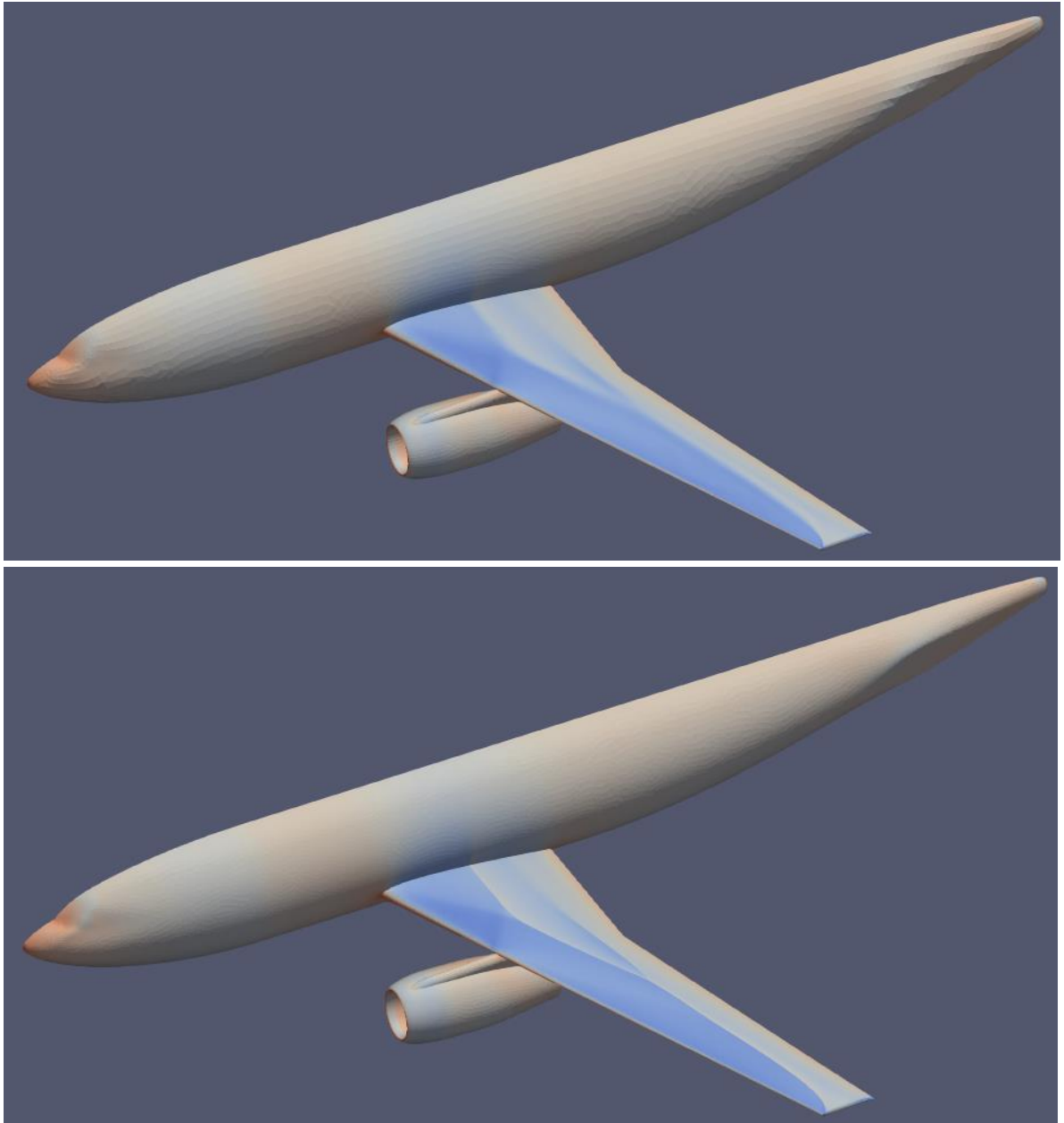


Figure 14: Surface pressure on the initial (top) and final (bottom) mesh cycles.

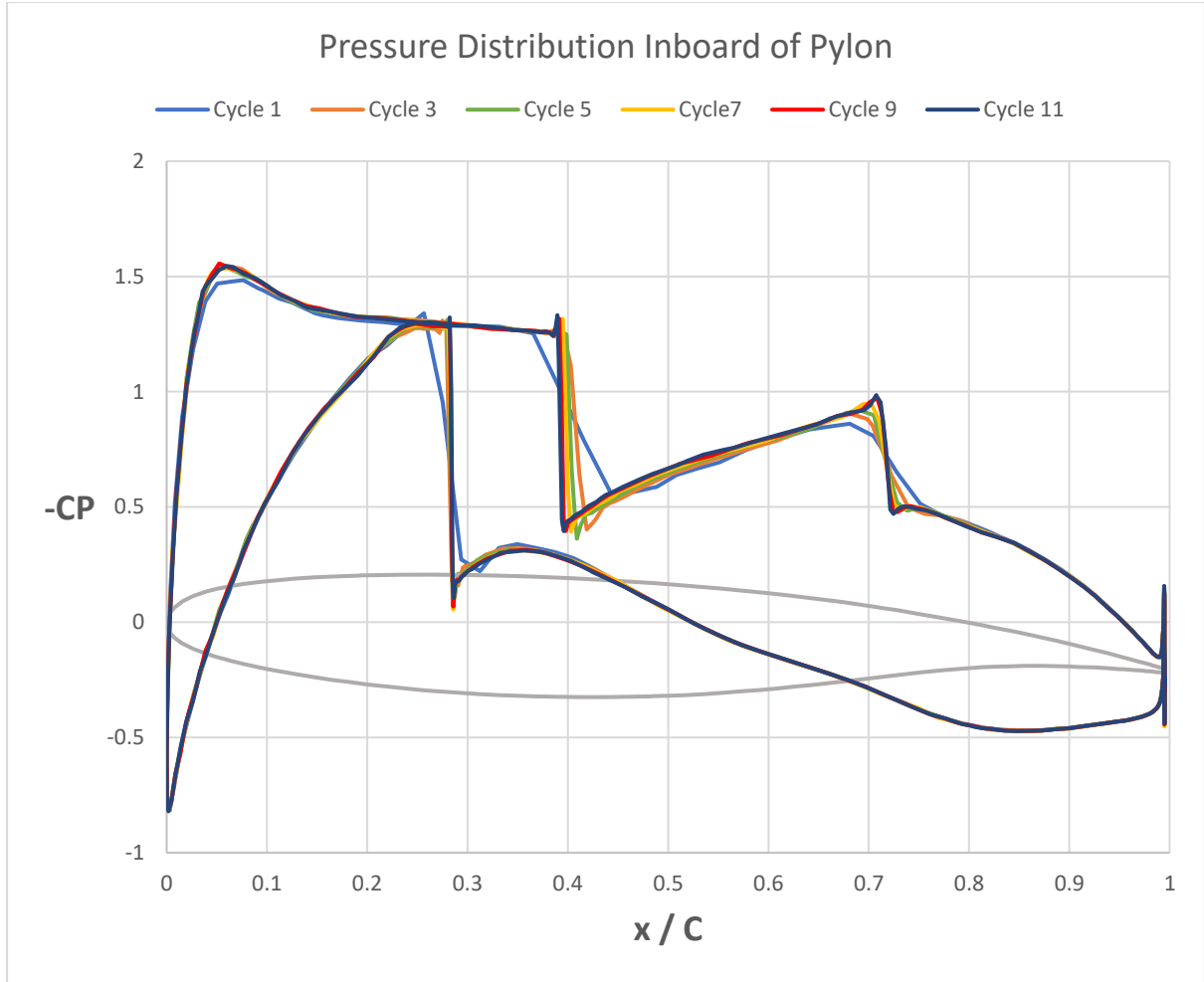


Figure 15: Pressure Coefficient at $N = 0.331$ station inboard of pylon. The shocks are refined as the cycles progress.

4 Unsteady Flows

Initial work has been done applying the mesh adaptation procedure to unsteady RANS solutions. The approach is best suited to periodic flows that feature bluff body wake shedding and cyclic inflow conditions. The described approach is modified to compute the adaptation sensor at each time step (Figure 16) over the period. The maximal sensor value is then retained at each location, and the maximal sensor field is then used to compute new target edge lengths for the adapted mesh. The new conformal mesh is then a fixed-grid improvement for the entire flow period. Repeated application of the procedure in cycles results in a final converged mesh suitable for the full unsteady period (Figure 17). As can be seen in Figure 18, small scale features in the unsteady flow are discovered and resolved. The approach demonstrated here also has application in turbomachinery blade row analysis.

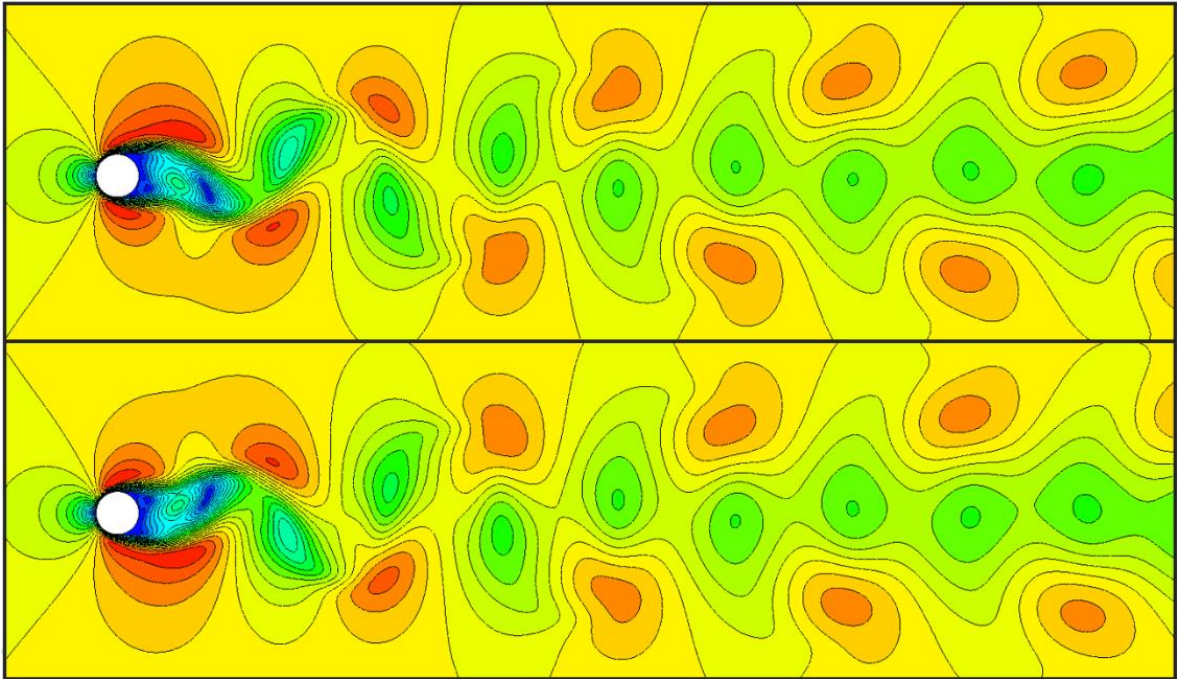


Figure 16: Unsteady vortex shedding behind a cylinder at the beginning (top) and mid-way (bottom) through the period.

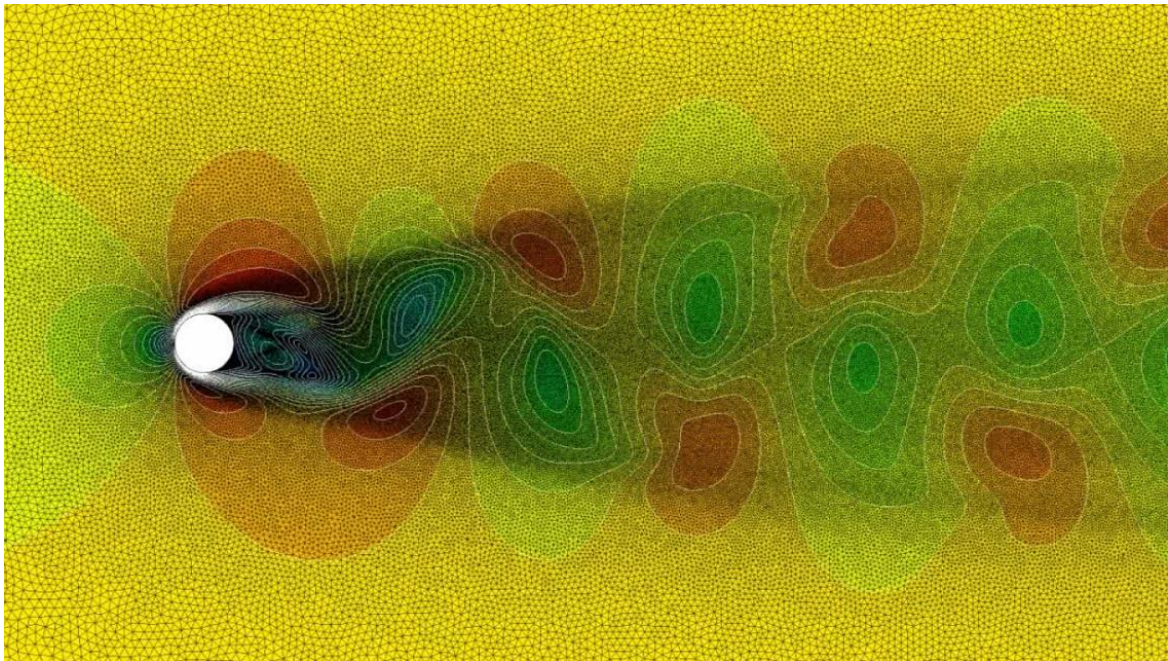


Figure 17: Mesh refinement of the entire unsteady wake region behind a cylinder.

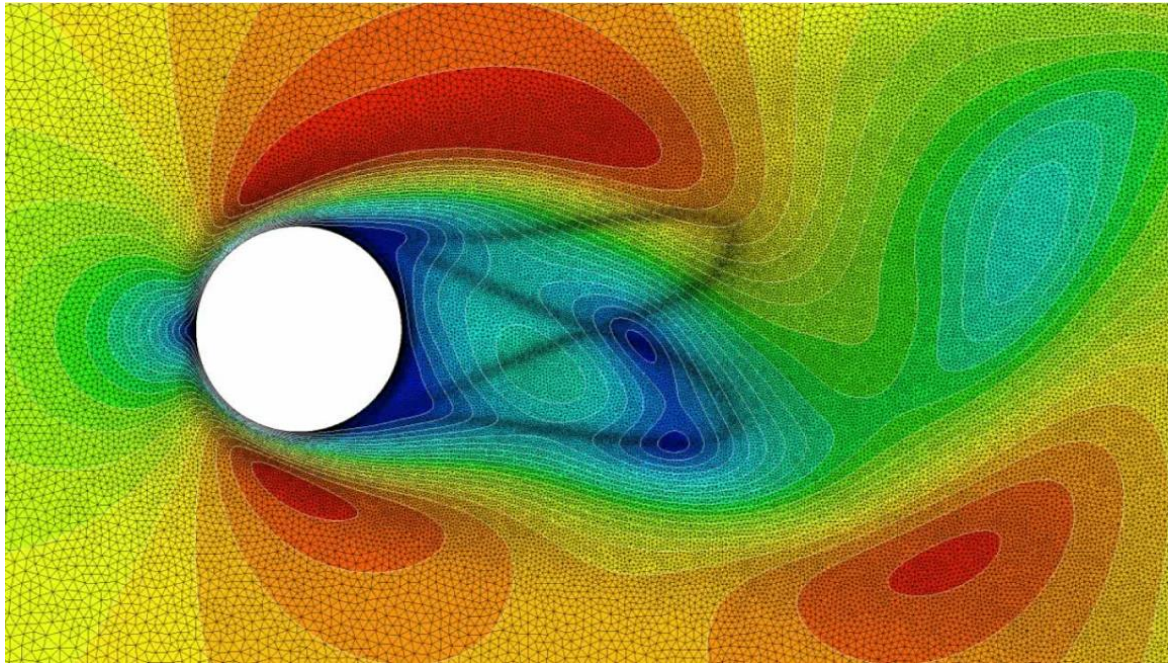


Figure 18: Enlarged view of the instantaneous solution and adapted mesh near the cylinder. Fine wake scales are recovered in the adapted mesh.

5 Conclusion and Future Work

A mesh adaptation procedure which maintains geometry associativity and anisotropic quasi-structured boundary layer mesh behavior has been developed and demonstrated on industrial cases. The method uses an estimate of truncation error of the discretization scheme to automatically control numerical error caused by the discrete mesh. The procedure was shown to be practical and computationally efficient on engineering problems while requiring minimal user intervention. Future work will include anisotropic adaptation in boundary layer and wake regions.

References

- [1] Slotnick, J., Khodadaoust, A., Alonso, J., Darmofal, D., Gropp, W., Lurie, E., Mavriplis, D., "CFD Vision 2030 Study: A Path to Revolutionary Computational Aerosciences," NASA Technical Report CR-2014-218178, 2014.
- [2] Derlaga, J.M. "Adjoint and Truncation Error Based Adaptation for Finite Volume Schemes with Error Estimates," 53rd AIAA Aerospace Sciences Meeting, Kissimmee, FL, January 2015.
- [3] Loseille, A. and Alauzet, F., "Continuous Mesh Framework Part I: Well-Posed Continuous Interpolation Error," SIAM Journal on Numerical Analysis, Vol. 49, No. 1, 2011, pp. 38-60.
- [4] Cooper, D., Jackson, D.C., Launder, B.E., Liao, G.X., "Impinging jet studies for turbulence model assessment. Part I: Flow-field experiments," Int. J. Heat Mass Transfer, Vol. 36, pp. 2675-2684, 1993.
- [5] Baughn, J.W., Yan, X., Masbah, M., "The effect of Reynolds number on the heat transfer distribution from a flat plate to an impinging jet," ASME Winter annual meeting, 1992.
- [6] Menter, F., Smirnov, P. E., Liu, T., Avancha, R., "A One-Equation Local Correlation-Based Transition Model," Flow Turbulence Combustion, Vol. 95(4), pp 1-37, 2015.
- [7] Walraevens, R., Gallus, H.E., "ERCOFTAC Testcase 6: 1-1/2 Stage Axial Flow Turbine," Institut für Strahltriebwerke und Turboarbeitsmaschinen, RWTH Aachen, Germany, 1997

- [8] Thomas D. Economon, Francisco Palacios, Sean R. Copeland, Trent W. Lukaczyk and Juan J. Alonso “SU2: An Open-Source Suite for Multiphysics Simulation and Design”, AIAA Journal 2016 54:3, 828-846
- [9] NASA, “Applied Aerodynamics Drag Prediction Workshop,” NASA, 2003. [Online]. Available: <https://aiaa-dpw.larc.nasa.gov/Workshop2/workshop2.html>. [Accessed: 15-Jun-2022].